

Multi-confound regression adversarial network for deep learning-based diagnosis on highly heterogenous clinical data

Matthew Leming^{1,*}, Sudeshna Das², and Hyungsoon Im^{1,3,†}

¹Center for Systems Biology, Massachusetts General Hospital, Boston, MA, USA

²Department of Neurology, Massachusetts General Hospital, Boston, MA, USA

³Department of Radiology, Massachusetts General Hospital, Boston, MA, USA

*Corresponding author: Matthew Leming, mleming@mgh.harvard.edu, 149 13th St., Charlestown, MA 02129

†Corresponding author: Hyungsoon Im, im.hyungsoon@mgh.harvard.edu, 149 13th St., Charlestown, MA 02129

May 9, 2022

Abstract

Automated disease detection in medical images using deep learning holds promise to improve the diagnostic ability of radiologists, but routinely collected clinical data frequently contains technical and demographic confounding factors that differ between hospitals, negatively affecting the robustness of diagnostic deep learning models. Thus, there is a critical need for deep learning models that can train on imbalanced datasets without overfitting to site-specific confounding factors. In this work, we developed a novel deep learning architecture, MUCRAN (Multi-Confounding Regression Adversarial Network), to train a deep learning model on highly heterogeneous clinical data while regressing demographic and technical confounding factors. We trained MUCRAN using 16,821 clinical T1 Axial brain MRIs collected from Massachusetts General Hospital before 2019 and tested it using post-2019 data to distinguish Alzheimer’s disease (AD) patients, identified using both prescriptions of AD drugs and ICD codes, from a non-medicated control group. In external validation tests using MRI data from other hospitals, the model showed a robust performance of over 90% accuracy on newly collected data. This work shows the feasibility of deep learning-based diagnosis in real-world clinical data.

Keywords: Deep learning, Magnetic Resonance Imaging, Alzheimer’s disease, Confounding factors

1 Introduction

Alzheimer’s disease (AD) is the leading cause of dementia, and with an aging population, the global burden is expected to increase [Association, 2021]. Current challenges in AD include the lack of a reliable means of early diagnosis, identification of high-risk groups, and frequent assessment of disease progression. Structural magnetic resonance imaging (MRI) is one of the five most important and established methods for measuring AD biomarkers [Vinters, 2015] and thus is useful in the initial evaluation of patients with suspected cognitive impairment [Knopman et al., 2021]. Early diagnosis of AD could have immense benefits for patients individually [Rasmussen and Langerman, 2019], allowing measures to be taken for the prevention or delay of disease progression, and would collectively save \$7 trillion in healthcare costs [Association, 2021].

The use of predictive AI to diagnose AD holds promise to automate, standardize, and apply this process at scale. Because clinical MRI is collected routinely, datasets are present that may be able to power predictive AI algorithms for

this purpose. Deep learning has shown success in detecting Alzheimer’s disease in high-quality MRI data collected in a controlled research setting [Wen et al., 2020]. However, implementing deep learning in clinical settings is hampered by practical challenges. Compared to images collected in research settings, clinical imaging data is often lower in quality and more diverse in technical variables, labeling, diseases, and patient populations. Furthermore, machines and clinical techniques used to acquire data differ between settings. Hence, a deep-learning model trained on clinical data from one hospital will not necessarily generalize to data from another. The large variations in technical and demographic variables, if not carefully processed, could lead to overfitting of a deep-learning model to these confounding factors rather than true biomarkers.

Implementing deep-learning models across hospitals requires a large degree of model robustness and ability to scale [Elemento et al., 2021]. This is a form of the out-of-distribution data problem [Lee et al., 2018] that is endemic in the field of deep learning. Data privacy concerns unique to healthcare make this problem especially difficult to overcome in diagnostic models, as the pooling of data in healthcare is yet infeasible from a policy standpoint. Sophisticated training strategies, such as federated learning [Dayan et al., 2021], in which models are trained internally in healthcare systems and subsequently released, address this robustness problem to an extent. However, it would be advantageous to develop models that use purely technical means, rather than organizational strategies, to regress confounding factors and thus address the out-of-distribution data problem for broader applications.

Several methods have been proposed to overcome the problem of confounded data. We have previously used a data matching scheme [Leming et al., 2022] to regress confounding factors in clinical MRI data by curating confounder-free, matched datasets for three-stage AD classification [Leming et al., 2022]. Data matching, however, causes the training set size to decrease as more confounding factors are included in the model. Zhao et al. proposed a confounder-free neural network trained using three optimizers in an adversarial scheme, demonstrating its effectiveness using scalar demographic confounding factors. [Zhao et al., 2020]. Similar adversarial methods to regress site differences have been used in the classification of cell batches [Kimmel and Kelley, 2021].

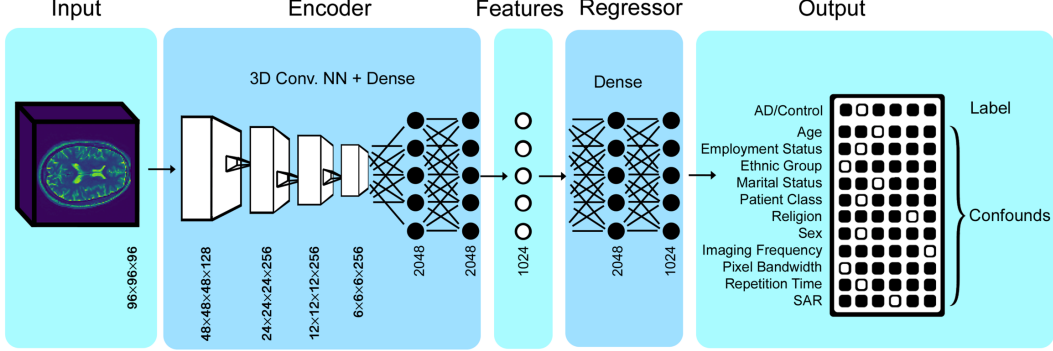
However, because new and unknown confounding factors could be introduced in a test set, confound regression models are not foolproof against out-of-distribution examples. Thus, for a real-world diagnostic system, uncertainty estimations that could detect out-of-distribution samples are necessary [Shad et al., 2021]. This has been a recent area of interest in deep learning [Lee et al., 2018], that has seen the development of sophisticated, built-in measures of uncertainty [Gal and Ghahramani, 2016, Liu et al., 2020, Gawlikowski et al., 2021]; however, more principled approaches, notably ensembles of independently trained models, are generally simpler to implement and easier understand, albeit more computationally intensive.

2 Materials and Methods

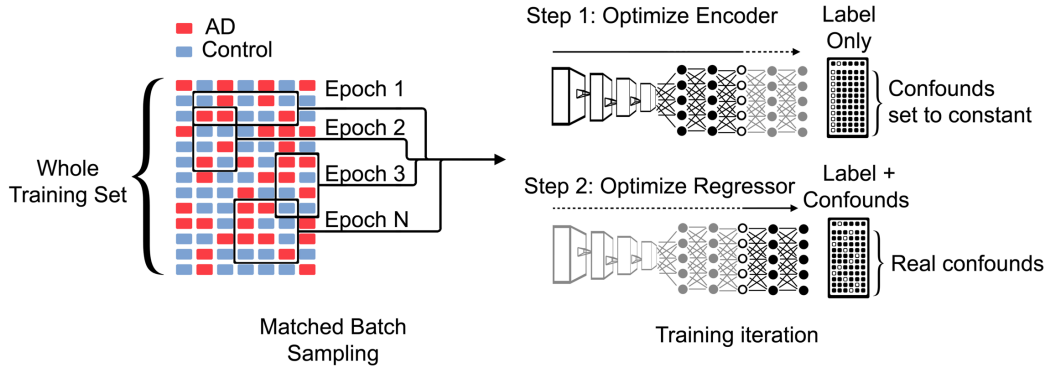
In this work, we developed the Multi-Confound Regression Adversarial Network (MUCRAN): an adversarial process on a specialized scheduler to train a model on a vast clinical MRI imaging dataset, while regressing recorded confounding factors (Figure 1). We applied the MUCRAN to distinguish between MRIs of Alzheimer’s disease (AD) patients and non-AD controls. The MUCRAN takes a 3D T1 Axial MRI as input and outputs binary labels for AD, as well as each confound included in the model (Figure 1A). In its training, the model is incentivized to classify an output disease label without the use of confounding factors. It is inspired by a confounder-free scheme [Zhao et al., 2020], though in its structure, it is more closely based on generative adversarial neural networks (GANs) [Goodfellow et al., 2014]. The MUCRAN consists of an encoder and regressor, similar to a generator and discriminator in conventional GANs, respectively (Figure 1B). The encoder translates input images to an intermediary feature representation, and the regressor translates these features to predictions of the disease label and confounding factors (e.g., age, sex, image modality), represented by an array of one-hot vectors. In the training scheme, back-propagation is applied to the regressor and encoder alternately using different output arrays; the regressor is trained using true output confound/label encodings, while the encoder is trained using the same label encoding, but false confound values (i.e., all of the one-hot vectors representing confounding factors are set to the same constant value). Thus, the encoder is incentivized to output an intermediary feature representation from which a true label can be derived without confounders.

To address the out-of-distribution data problem in large clinical data, we also implemented a consensus approach,

A. Model



B. Training



C. Testing

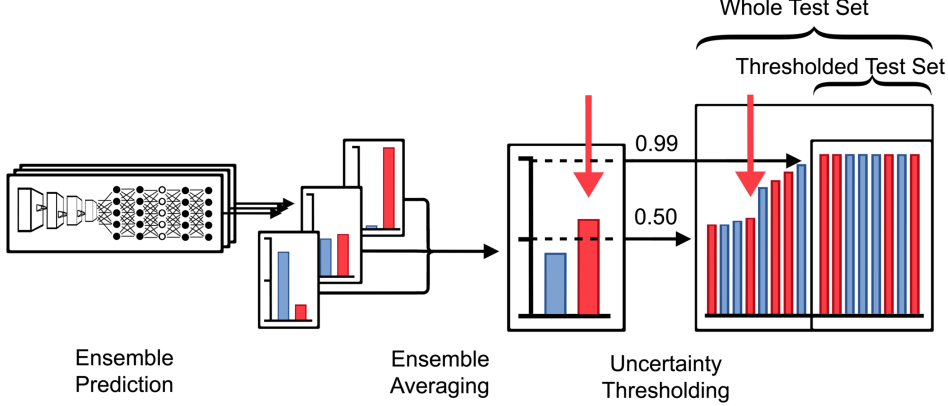


Figure 1: Multi-Confound Regression Adversarial Network (MUCRAN). A. MUCRAN is a convolutional neural network (CNN) that takes a $96 \times 96 \times 96$ MRI as input, encodes it to an array of 1024 intermediary features via a CNN and a dense neural network, and regresses these features to an output array. The output array consists of one-hot binary vectors that encode both the primary label (AD/Control) and included confounding factors (sex, age, and so on). B. For training the regressed model, large batches are sampled from an imbalanced dataset such that AD and control are present in equal proportions. For each training iteration, the model is trained in a two-step adversarial process: with the regressor frozen, the encoder is fit to an output array with the label set to its real value, but each confound row set to a constant value ($[1, 0, 0, \dots, 0]$); the regressor is then fit to the array with both the label and its true confound values. C. For testing, labels are predicted through multiple independent models, and their votes are averaged into an ensemble vote. An uncertainty thresholding is then applied to isolate an in-distribution test set.

motivated from clinical practice for AD diagnosis, by using an ensemble of models to separate out-of-distribution cases in test sets (Figure 1C). These features enabled us to construct a robust model for detecting AD cases using clinical MRI data. For external validation, we applied MUCRAN for MRI data from hospitals different from the one used for model training. We also tested newly collected images to test the feasibility of the model for future clinical implementation.

2.1 Data

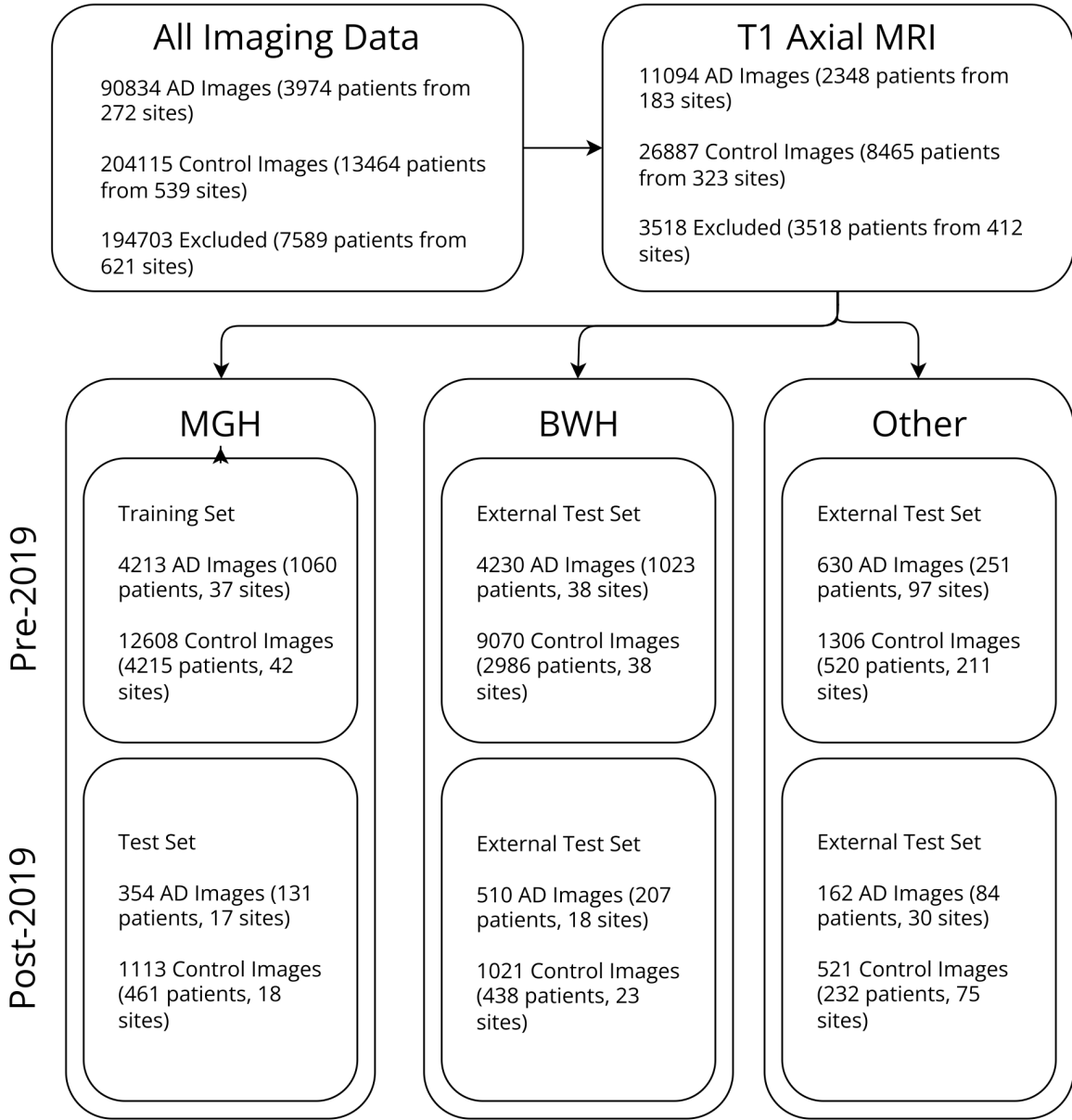


Figure 2: Statistics associated with the three datasets used, pre- and post-2019. T1 Axial MRI, representing the plurality of structural MRI in the Mass General Brigham database, were taken from our full database of imaging data, and, from these, three test sets were isolated. Patients with lesions, head trauma, or tumors, including all data from the Dana Farber Cancer Institute, were excluded.

Descriptions of the full dataset can be seen in Figure 2. MRI data were requested from the Mass General Brigham Research Patient Data Registry (RPDR), and additional variables were augmented from the Enterprise Data Ware-

house (EDW), which stored additional patient metadata but no images. Data were separated into three sets: MGH, BWH, and Other (i.e., miscellaneous data which was imported by patients from outside hospital systems).

The presence of Alzheimer's disease was assumed by analyzing patient medication records, in particular the presence of Galantamine, Rivastigmine, Donepezil, or Memantine, or an ICD 10 code of G35. While medication does not constitute a precise diagnosis of Alzheimer's, it was more consistently recorded across the database than ICD codes. Patients with history of previous head trauma or malignant neoplasms were removed from consideration, and all data from the Dana Farber Cancer Institute were removed, due to the high likelihood of cancer patients.

2.2 Preprocessing

Due to the size and variability of the dataset, preprocessing was limited to translating images from DICOM to Nifti (dcm2niix), reorienting them to a standard space (fsorient2std), and resizing them to a standard $96 \times 96 \times 96$ dimension. Diversity of the dataset led to a number of preprocessing errors, and so a number of criterion were made to include data, notably the size of the file (i.e., files that were too small were excluded from consideration). (These technical "exclusions" are not included in Figure 1.) Dataset size and variability prevented the application of conventional MRI preprocessing methods, such as registration to a template.

Over 100 associated technical and demographic variables were included in the dataset, but only a few were usable as confounding factors that could be encoded. Labels and confounding factors were encoded as 2D arrays of binary, one-hot vectors, with each row representing a category or value range, as well as an extra row to indicate data with missing or null values.

2.3 ML Model and training

A diagram of the model used for our training can be seen in Figure 1. Our model is incentivized to classify by an output disease label without the use of confounding factors. The structure is similar to generative adversarial neural networks (GANs) [Goodfellow et al., 2014]. Briefly, GANs are incentivized to generate photorealistic images using a generator, which outputs the images, and a discriminator, which is trained to discriminate between real images and the generator's outputs; by training both in an adversarial process, the generator eventually outputs images that the discriminator is unable to distinguish. In this model, the "generator" is an encoder that translates input images to an intermediary feature representation, while the "discriminator" is a regressor that translates these features from the intermediary feature representation to predictions of the disease label, as well as a number of confounding factors (i.e., age, sex, image modality). The regressor is trained using true output confound/label encodings, while the encoder is trained using the true label encoding, but confound encodings that are all set to the same value. Thus, the encoder is incentivized to output an intermediary feature representation from which a true label, but no confounding factors, can be derived.

Put formally, suppose we have input data, x , a label, y , with possible values y_1, y_2, \dots, y_N , and a number of confounds, c^1, c^2, \dots, c^K , each with possible values $c_1^i, c_2^i, \dots, c_N^i$. The encoder, E , outputs intermediary features, $E(x) = F$, while the regressor, R , outputs a vector that combines the label and confounds, such that $R(F) = p([y, c^1, c^2, \dots, c^K])$. The loss function of the encoder is:

$$Loss(E(x)) = \begin{bmatrix} W \\ 1 \\ 1 \\ \vdots \\ 1 \end{bmatrix} \cdot \frac{-1}{N} \cdot \sum_{i=1}^N \left(\begin{bmatrix} y_i \\ G(i) \\ G(i) \\ \vdots \\ G(i) \end{bmatrix} \cdot \log(R(E(x))) + 1 - \begin{bmatrix} y_i \\ G(i) \\ G(i) \\ \vdots \\ G(i) \end{bmatrix} \cdot \log(1 - R(E(x))) \right) \quad (1)$$

Where

$$G(x) = \begin{cases} 1, & \text{if } x = 1 \\ 0, & \text{if } x \neq 1 \end{cases}$$

While the loss function of the regressor is:

$$\text{Loss}(R(x)) = \begin{bmatrix} W \\ 1 \\ 1 \\ \vdots \\ 1 \end{bmatrix} \cdot \frac{-1}{N} \cdot \sum_{i=1}^N \left(\begin{bmatrix} y_i \\ c_i^1 \\ c_i^2 \\ \vdots \\ c_i^K \end{bmatrix} \cdot \log(R(E(x)) + 1 - \begin{bmatrix} y_i \\ c_i^1 \\ c_i^2 \\ \vdots \\ c_i^K \end{bmatrix} \cdot \log(1 - R(E(x)))) \right) \quad (2)$$

These are both modified binary crossentropy loss functions. To ensure its convergence, the y label is given an additional weighting factor, W (in practice, this is set to 6).

The similarity of these models to GANs allowed us to draw on the wide body of research and conventions used to train them [Chintala et al., 2016, Radford et al., 2016, Salimans et al., 2016]. The encoder was trained using an Adam optimizer, while the regressor was trained using an SGD optimizer. Sparse gradients, such as ReLU and max pooling, were avoided in the construction of the networks. The use of an adversarial system placed certain limitations on which layers could be used; for instance, pooling layers were removed in favor of strided convolutions, and batch normalization layers had to be avoided at the output of the encoder and input of the regressor [Radford et al., 2016].

In this work, two classes of models were trained, which are referred to as "confounded" and "regressed". These were each created by modifying the loss function of the encoder and regressor. The regressed versions were trained using the loss functions as presented above (i.e., Equation 1 for the encoder and equation 2 for the regressor); the confounded versions were trained using equation 2 for both the encoder and regressor. Thus, the regressed model was the only one trained using a truly adversarial process.

2.4 Batch scheduler

Training was not performed in epochs over the whole training set, as is typically the case. Rather, it was implemented using a scheduler that maintained equal ratios in any given batch between AD and control data. The scheduler constructed individual batches, half with equal ratios between classes of the label, and the other half with equal ratios of iterative confounding factors (thus, one batch would have 50% composed of data that is half Alzheimer's and half control, while the other 50% would have equal ratios of male and female; the next batch would have 50% that is half Alzheimer's and half control and 50% with equal distributions of age; and so on). 48 MRIs of these batches would then be loaded into main memory at a time and trained for five iterations in random order. After a batch had been completely loaded and discarded from main memory, a new one would then be sampled. This process was repeated until 100,000 datapoints had been loaded and trained on.

The two model classes (confounded and regressed) were trained side-by-side to make them more comparable. For a given model in the regressed ensemble, there is a corresponding model in the confounded ensemble that was trained on the exact same schedule in the same order.

2.5 Consensus approach using ensemble models

We show the differences in model accuracy on an entire test set and just the "in-distribution" portion. A test set consisting of in-distribution and out-of-distribution data will output a mix of certain predictions (for in-distribution data) and uncertain predictions (for out-of-distribution data – or, possibly, genuine "close calls" between AD and control data). As individual measurements are averaged across an ensemble of models, averaged in-distribution measurements will tend towards either 0.0 or 1.0, while averaged out-of-distribution measurements will tend towards

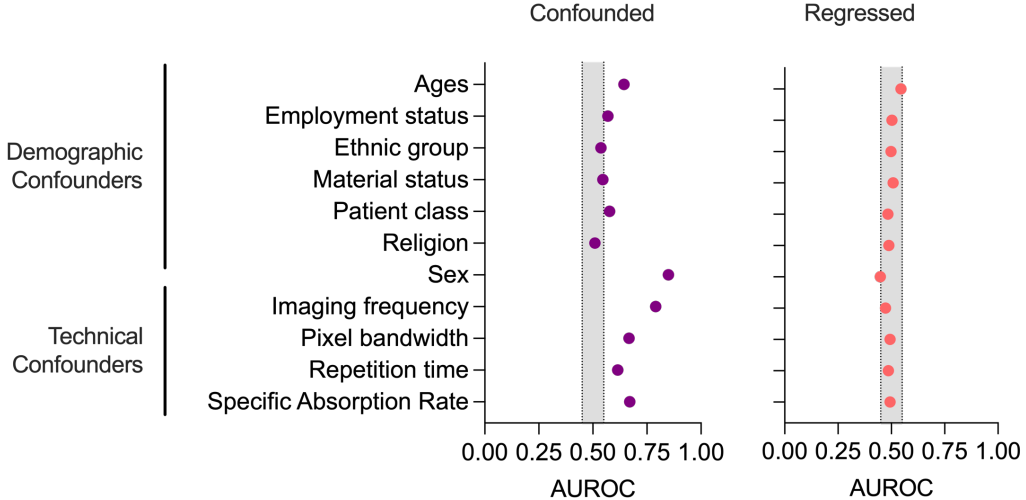


Figure 3: Prediction of confounding factors. Averaged results of model performance for predicting demographic and technical confounding factors were reported as area under the receiver operating characteristics (AUROC) for the confounded and regressed ensembles.

0.5, if the outputs are essentially random. Thus, after averaging predictions using an ensemble of models, in-distribution measurements can be isolated by removing outputs with an average that falls below a certain output value (i.e., varies across ensembles). We show the accuracy of this model, from the inclusion of all data to the exclusion of all but the most certain datapoints in the test set. Net accuracy can additionally be increased on a per-patient basis by averaging each MRI particular to individual patients. See Figure 1C.

2.6 Gradient Class Activation Maps

We compare the results of an ensemble of models trained to regress confounding factors to those trained to predict confounding factors. To further analyze these results, we show the gradient class activations [Simonyan et al., 2014, Selvaraju et al., 2017] averaged over 100 random images in each model’s test set set, then averaged across each ensemble. This shows where in the image, on average, models focus when making their classification decision. Image features not relevant to technical variables but not the disease in question may be gleaned by looking at the periphery of an image, while true biomarkers may be gleaned only by looking at the brain, which is in the center of an MRI. This shows that one of the mechanisms by which regression operated was to focus the attention of the network onto true biological areas rather than background features. Thus, this is an indirect test of how well the proposed regression methods focus the model’s attention to biomarkers.

3 Results

We trained the MUCRAN with T1 Axial MRI data from Massachusetts General Hospital (MGH, $n = 16,821$, from 8780 unique scanning sessions; see supplementary information, Table S1, for a list of sites used in the training set) collected between 1995 and 2018 (Pre-2019, Figure 2). We kept the MGH data collected between 2019-2021 (Post-2019, $n = 1,467$) out of the training and used it as an internal test set. In training, we used large batches sampled with equal numbers of AD and control groups. We then used clinical MRI data Brigham and Women’s Hospital (BWH) as well as miscellaneous external hospitals, both with the same time divisions, for external validation.

Table 1: Results when the whole test set is included (threshold = 0.5), and results for which the averaged prediction in its respective category is above 0.99 (i.e., each model in the ensemble unanimously agrees). Shown are the accuracies on the portion of the dataset included after thresholding, and the size of that test set (in parentheses). See also Figure 1 C.

Threshold	Method	MGH		BWH		Others		All
		Post-2019	Pre-2019	Post-2019	Pre-2019	Post-2019	Post-2019	
0.99	Regressed	92.2% (628)	86.3% (5297)	91.5% (539)	89.5% (848)	95.2% (335)	86.9% (7958)	
	Confounded	88.8% (760)	85.5% (6565)	90.0% (671)	88.0% (1031)	92.1% (382)	85.3% (9892)	
0.50	Regressed	76.2% (1467)	73.2% (13300)	75.8% (1531)	75.7% (1936)	81.2% (683)	72.7% (20860)	
	Confounded	78.5% (1467)	73.4% (13300)	75.2% (1531)	75.9% (1936)	82.5% (683)	72.8% (20860)	

3.1 Comparison between confounded and regressed models

Of the 141 variables present in the dataset, eleven confounding factors were selected to be regressed from the model: age, employment status, ethnic group, marital status, patient class (e.g., inpatient or outpatient), religion, sex, specific absorption rate, imaging frequency, pixel bandwidth, and repetition time. Several criteria were considered in the selection of these confounding factors, including (1) their variance and distribution across T1 Axial MRIs (single-valued confounding factors were present and not included); (2) a low number of categorical choices, which made it practically encodable; (3) their presence across a large amount of data; (4) their theoretical relevance to both site differences and AD; and (5) their likelihood of being predicted from MRI, with confounding factors that were likely to be predicted from MRI (i.e. sex) and unlikely (i.e. religion) both included as a means of comparison.

Figure 3 shows model performance for predicting demographic and technical confounding factors on two sets of ensembles, one in which confounding factors were regressed (Regressed) and one in which they were predicted directly (Confounded); due to imbalances in proportions of values that could distort prediction accuracy, these are reported in the area under the receiver operating characteristics (AUROC). In the confounded model, some confounding factors, such as age, sex, imaging frequency, pixel bandwidth and specific absorption rate, could be predicted very effectively by the model, while others, such as religion and ethnic group, could not. However, in our regressed model, it shows that the AUROCs for all confounding factors are within the 10% margin from 0.5. This indicates that the regressed model fails to predict confounding factors using MRI data, and thus the adverse effects from confounding factors are minimized.

We further compared the differences between confounded and regressed models by visualizing the areas each model focused on using gradient class activation mapping [Simonyan et al., 2014, Selvaraju et al., 2017] (Grad-CAM, Figure 4). From a randomly selected 100 images, the confounded model focused more on areas outside of the brain than inside of the brain. This is likely due to overfitting of the model to technical variables, since technical variables could more readily be discerned by analyzing areas of the image without biological information. Because the brain appears in the middle of the image in MRIs, these areas would be the edges. In contrast, the regressed models have, on average, five-fold higher activation on the brain area. This shows that regression tends to focus on biological rather than technical markers. However, while the edge area was reduced by approximately half between the confounded and regressed models, it was not completely removed, which indicates that the regression process, while effective, may be imperfect; this could be due to confounding factors that were either unrecorded or not included in the regression process.

3.2 Consensus approach using ensemble models

To evaluate our test sets, a consensus approach is applied that separates out-of-distribution data (data that is a close-call between AD and control) from in-distribution data (Figure 1C). Ten models are trained independently in an ensemble; for each point evaluated in the test set, a prediction for AD and control is output; after a softmax layer, the sum of these predictions is normalized to 1. These ten predictions are averaged across the ensemble, and the averaged prediction with the higher value is taken as the final prediction for that datapoint; this averaged prediction falls in the range between 0.5 and 1.0.

A threshold may be applied to exclude from consideration those averaged predictions that fall below a certain value;

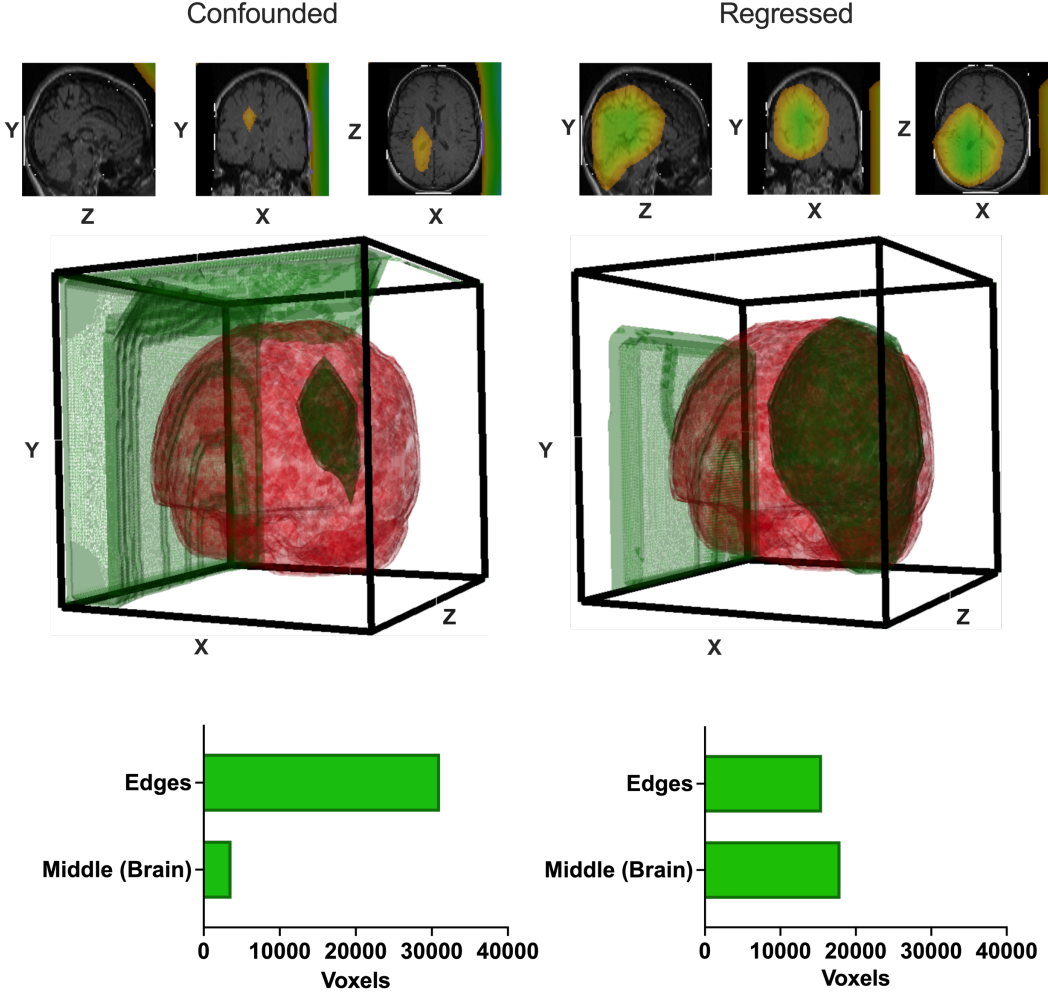


Figure 4: Averaged gradient class activation map results. A. Gradient-weighted class activation mapping (Grad-CAM) results for confounded and regressed models, thresholded at 0.15. The regressed model, in which confounding factors were regressed, shows higher activations inside the brain than the confounded model. B. A 3D mesh representation of the Grad-CAM data; a glass brain (in red) is included for visualization purposes. C. Total voxels in each ensemble covering the middle (brain) and edge areas.

in practice, this raises the classification accuracy substantially. Table 1 shows the result when this threshold is set to 0.5, effectively including all of the datapoints, as well as 0.99, including only those datapoints that all of the models in the ensemble set at 1.0.

In practice, this thresholding substantially increased classification accuracy of data that falls above the threshold. For the post-2019 MGH test data, the accuracies for the whole data set (threshold = 0.5) remain under 80%. However, with a higher threshold (0.99) applied, the accuracies were improved more than 10%, and the regressed model outperformed the confounded model (92.2% vs. 88.8%). Notably, this higher accuracy comes out on a smaller test set (92.2% from 628 data vs. 76.2% from 1467 data) after excluding the "out-of-distribution" data. This is likely indicative that individual regressed models did not show higher accuracy, but rather that the regressed ensemble is more skeptical about making "bad hires" for its in-distribution pool.

3.3 External validation

Table 1 also shows the results on the four external test sets considered — BWH and Other (miscellaneous) hospitals, each pre- and post-2019 (Figure 2). They share none of the same imaging sites as the MGH data, and so the confounded models are less able to utilize site-specific details in making their evaluations. This is reflected by a smaller difference between regressed and confounded models when the MUCRAN was tested with the whole test set (threshold = 0.5). With the thresholded (threshold = 0.99) datasets, the regressed ensemble showed high accuracies over 85% while outperforming the confounded ensemble in each case. This shows that, even in outside hospital systems, the regressed ensemble is able to show superior discrimination ability when separating out-of-distribution from in-distribution data in its classification. Furthermore, the MUCRAN showed over 90% accuracies across different hospitals for newer data sets obtained post-2019 with a maximum accuracy of 95.2%.

4 Discussion

4.1 MUCRAN regressed confounders and showed reliable prediction accuracy across hospitals

This work focused on designing a model disincentivized from incorporating confounding information in its classification. Unlike research settings where large amounts of data are curated for certain deep learning tasks, clinical data represent highly heterogeneous, often poorly-organized sets that contain many different confounders. With MUCRAN, we addressed the issue of confounding factors by designing adversarial networks to regress and minimize their influence in the model performance.

The presence of confounding factors in data does not necessarily mean that a given deep learning model is able to detect these confounding factors (see Figure 3, in which the confounded model failed to predict several of the confounding factors) or that, if it can, it utilizes them in an undesirable way when making its decision on the classification. Furthermore, measuring the effects of confounding factors on label classification is challenging because the use of confounding factors could either artificially increase test set accuracy, as our confounded model did on the MGH post-2019 dataset (Table 1, threshold = 0.5) or decrease it due to poor robustness, as the confounded model did on the external validation datasets (Table 1, threshold = 0.99). This is a form of the black-box problem that hinders the implementation of deep learning models in clinical settings.

Besides analyzing accuracies on different datasets and thresholds, another way we addressed the black box problem was by using gradient class activation maps. We used Grad-CAMs to show that the proposed model tended to focus on biomarkers and not technical confounding factors that could be gleaned by looking at the image periphery, more so than models trained to predict confounding factors directly. While this did not necessarily determine whether or not these were true biomarkers of AD (for instance, demographic variables, such as age, are confounding factors that could presumably be gleaned by focusing on the brain rather than the image periphery), our results did indicate that the regressed model refocused itself on areas of the input image relevant to purely biological information (Figure 4).

We also implemented an uncertainty measurement scheme to remove "uncertain" cases from the test set, as quantified by the average value of a measurement across an ensemble of models. This method is analogous to clinical practice of in the diagnosis of AD, in which a group of clinicians review patient information and test results to make a consensus to determine the stage of AD or cognitive impairment. This approach showed an extremely high model efficacy on those remaining in-distribution datapoints, making a strong case for use of this diagnostic technology in a clinical setting.

In our external validation tests using data from BWH and other hospitals, the MUCRAN showed a similar level of accuracy to the MGH dataset. It also showed a consistently higher accuracy than confounded models. A likely reason for this is that the confounded models relied on consistently-present technical confounding factors for their predictions, which made them more certain of wrong predictions, whereas the regressed ensemble, incentivized to rely on true biomarkers, was not biased in such a way. This idea is supported by the fact that the greatest difference in accuracy is found in the "other" set, which has a greater variety of different sites than the BWH and MGH sets. The results show that the use of uncertainty measurements, removing data that appears to be "out-of-distribution",

provides a framework that makes diagnostic AI scalable in the real world. AI that can provide predictably accurate and useful diagnoses to a portion of in-distribution data, while detecting and removing itself from consideration of out-of-distribution data, is more useful than AI that makes a blanket prediction on all datasets, regardless of certainty.

4.2 Development and context of MUCRAN

The model was inspired by the confounder-free architecture described in Zhao et al. 2020, and in early stages of this project, this model was re-implemented and tested. Our alterations to this constitute the contribution on the pure machine learning side of this project and brought our model closer to more commonly used adversarial models, which allowed us to draw on the extensive research in that area when implementing training schemes. Zhao et al. 2020 relied on an inverse loss function to disrupt the classifier's prediction of confounding factors. This required a third optimizer. In early tests, we found that the third optimizer and the inverse loss function disrupted convergence during training, frequently leading to mode collapse, especially when more than one confound was included in the training scheme. In contrast, our adversarial approach relies on incentivizing the encoder to fool the regressor into classifying all confounding factors as one specific value. This allowed us to use one loss function (binary crossentropy) and many different confounding factors simultaneously. Thus, we combined the label and confounding factors into one representation (the 2D array of one-hot vectors), rather than training a separate network for each, and used two optimizers, which aided in network convergence.

MUCRAN is designed for contexts in which data is highly complex and confounded, but for which these confounding factors are recorded. This makes it uniquely suited to medical imaging data. While this most likely limits its use in common deep learning tasks involving photographic images and natural language processing, the architecture may readily be adapted for training on imaging data from any field that needs to incorporate imaging data from multiple sites and machines.

Extensive testing was performed on more sophisticated network architectures. However, with the adversarial training process, more complex CNNs, such as ResNet, DenseNet, and InceptionNetV3, failed to converge, or simply performed worse than the simple layered CNN used in this work (Figure 1A). Extensive testing was also performed on the method of sampling training data. Training schemes that followed more closely the typical one, in which the whole training set is fed to the model sequentially, led to overfitting. One source of this model's success is likely the batch training scheme used (explained further under "Methods - Batch Scheduler"). By continuously sampling batches from a larger pool of data, new datapoints are continuously introduced to the model throughout its training, which discourages overfitting.

4.3 Further improvements on cross-institutional clinical testing

The deep learning task presented was challenging from a bioinformatics perspective. The inference of Alzheimer's disease in clinical records is difficult because they are often improperly labeled; ICD codes may be incomplete, and data recording practices vary with databases, clinics, time periods, and medical practitioners. While it is an imperfect marker, the use of medications as a label marker was advantageous because (1) the four medications used in this study are used to treat Alzheimer's in its different stages (though Memantine is sometimes used in younger age groups [Hosenbocus and Chahal, 2013]) and (2) prescriptions are consistently recorded in the electronic health record. We included, as well, instances in which an ICD indicating Alzheimer's was recorded but not a medication.

While most deep learning tasks present one straightforward metric to improve — accuracy — the current study presents two: both accuracy and test set inclusion. Overall, the regressed model, after thresholding, made predictions on an in-distribution dataset consisting of 7958/20860 datapoints, or 38.1% of the data (Table 1), at 86% accuracy (though, considering only post-2019 data, which omits much of the lower-quality legacy MRIs in the dataset, this percentage rises to above 90% in all cases). On the one hand, accurate predictions on 38.1% of MRIs at a given hospital for routinely-collected MRI would be a useful metric for radiologists to consider; on the other hand, this still omits over half of all data. Even so, unlike a system that measures every datapoint considered, whether or not it is in- or out-of-distribution, ensembles of MUCRANs, by offering fewer unreliable predictions, present a system

that can be implemented and scaled in the real world.

In conclusion, we present deep learning methods that are able to generalize across dates and hospitals for diagnosing Alzheimer's disease in complex clinical MRI. We also show a means of separating out-of-distribution data that cannot be effectively assessed by our models from in-distribution data that can, providing a scalable AI system that can be deployed in new environments.

Data availability

The clinical data utilized in this study is not publicly available because it contains confidential information that may compromise patient privacy as well as the ethical or regulatory policies of our institution. A part of data will be made available on reasonable request by contacting the corresponding author (H.I. im.hyungsoon@mgh.harvard.edu) upon the approval from institutional review boards.

Code availability

Our code used in this study is publicly available at <https://github.com/mleming/MUCRAN>.

References

- [Association, 2021] Association, A. (2021). 2021 alzheimer's disease facts and figures. *Alzheimers Dement*, 17.
- [Chintala et al., 2016] Chintala, S., Denton, E., Arjovsky, M., and Mathieu, M. (2016). How to train a gan? tips and tricks to make gans work. *NIPS2016*.
- [Dayan et al., 2021] Dayan, I., Roth, H., Zhong, A., et al. (2021). Federated learning for predicting clinical outcomes in patients with covid-19. *Nature Medicine*, 27:1735–1743.
- [Elemento et al., 2021] Elemento, O., Leslie, C., Lundin, J., and Tourassi, G. (2021). Artificial intelligence in cancer research, diagnosis and therapy. *Nature Reviews Cancer*, 21:747–752.
- [Gal and Ghahramani, 2016] Gal, Y. and Ghahramani, Z. (2016). Dropout as a bayesian approximation: Representing model uncertainty in deep learning. *Proceedings of the 33 rd International Conference on Machine Learning*, 48.
- [Gawlikowski et al., 2021] Gawlikowski, J., Tassi, C., Ali, M., Lee, J., Humt, M., Feng, J., Kruspe, A., Triebel, R., Jung, P., Roscher, R., Shahzad, M., Yang, W., Bamler, R., and Zhu, X. (2021). A survey of uncertainty in deep neural networks. *arXiv*.
- [Goodfellow et al., 2014] Goodfellow, I., Pouget-Abadie, J., Mirza, M., Xu, B., Warde-Farley, D., Ozair, S., Courville, A., and Bengio, Y. (2014). Generative adversarial nets. *Advances in Neural Information Processing Systems* 27, page 2672–2680.
- [Hosenbocus and Chahal, 2013] Hosenbocus, S. and Chahal, R. (2013). Memantine: A review of possible uses in child and adolescent psychiatry. *J Can Acad Child Adolesc Psychiatry*, 22:166–171.
- [Kimmel and Kelley, 2021] Kimmel, J. and Kelley, D. (2021). Semi-supervised adversarial neural networks for single-cell classification. *Genome Res*, 31:677–688.
- [Knopman et al., 2021] Knopman, D., Amieva, H., Petersen, R., Chételat, G., Holtzman, D., Hyman, B., Nixon, R., and Jones, D. (2021). Alzheimer disease. *Nat Rev Dis Primers*, 7:33.
- [Lee et al., 2018] Lee, K., Lee, K., Lee, H., and Shin, J. (2018). A simple unified framework for detecting out-of-distribution samples and adversarial attacks. *arXiv*, 1807.03888.

[Leming et al., 2022] Leming, M., Das, S., and Im, H. (2022). Construction of a confounder-free clinical mri dataset in the mass general brigham system for classification of alzheimer’s disease. *Artificial Intelligence in Medicine*, 129.

[Liu et al., 2020] Liu, S., Yadav, C., Fernandez-Granda, C., and Razavian, N. (2020). On the design of convolutional neural networks for automatic detection of alzheimer’s disease. In Dalca, A. V., McDermott, M. B., Alsentzer, E., Finlayson, S. G., Oberst, M., Falck, F., and Beaulieu-Jones, B., editors, *Proceedings of the Machine Learning for Health NeurIPS Workshop*, volume 116 of *Proceedings of Machine Learning Research*, pages 184–201. PMLR.

[Radford et al., 2016] Radford, A., Metz, L., and Chintala, S. (2016). Unsupervised representation learning with deep convolutional generative adversarial networks. *ICLR*.

[Rasmussen and Langerman, 2019] Rasmussen, J. and Langerman, H. (2019). Alzheimer’s disease – why we need early diagnosis. *Degener Neurol Neuromuscul Dis.*, 9:123–130.

[Salimans et al., 2016] Salimans, T., Goodfellow, I., Zaremba, W., Cheung, V., Radford, A., and Chen, X. (2016). Improved techniques for training gans. *arXiv*.

[Selvaraju et al., 2017] Selvaraju, R., Cogswell, M., Das, A., Vedantam, R., Parikh, D., and Batra, D. (2017). Grad-cam: Visual explanations from deep networks via gradient-based localization. *2017 IEEE International Conference on Computer Vision (ICCV)*.

[Shad et al., 2021] Shad, R., Cunningham, J., Ashley, E., Langlotz, C., and Hiesinger, W. (2021). Designing clinically translatable artificial intelligence systems for high-dimensional medical imaging. *Nature Machine Intelligence*, 3:929–935.

[Simonyan et al., 2014] Simonyan, K., Vedaldi, A., and Zisserman, A. (2014). Deep inside convolutional networks: Visualising image classification models and saliency maps. In *Workshop at International Conference on Learning Representations*.

[Vinters, 2015] Vinters, H. (2015). Emerging concepts in alzheimer’s disease. *Annu. Rev. Pathol. Mech. Dis.*, 10:291–319.

[Wen et al., 2020] Wen, J., Thibeau-Sutre, J., Diaz-Meloe, M., Samper-González, J., Routiere, A., Bottanie, S., Dormonte, D., Durrelman, S., Burgos, N., and Colliota, O. (2020). Convolutional neural networks for classification of alzheimer’s disease: Overview and reproducible evaluation. *Medical Image Analysis*, 63.

[Zhao et al., 2020] Zhao, Q., Adeli, E., and Pohl, K. (2020). Training confounder-free deep learning models for medical applications. *Nature Communications*, 11.

Supplementary Information

Uncertainty thresholds

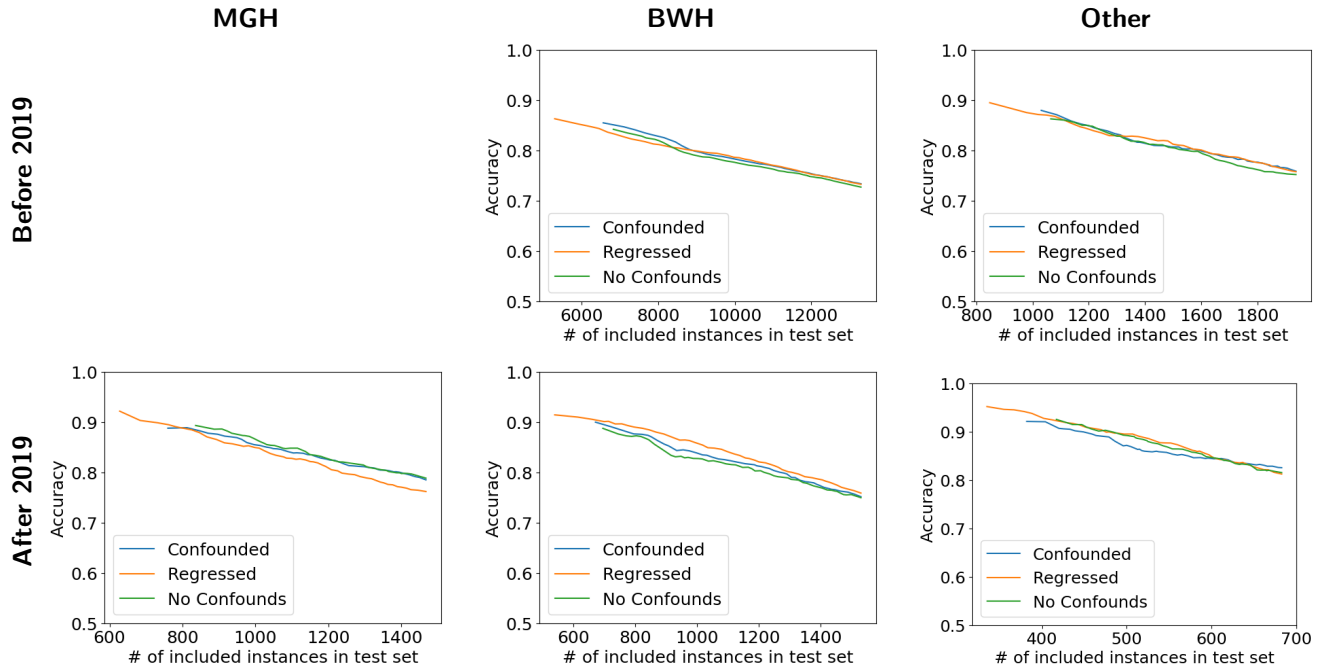


Figure S1: Relative accuracy of each ensemble in threshold values between 0.00 and 0.99. Lines on these graphs show the intermediate accuracies and number of included datapoints in each test set for values between 0.00 and 0.99; see table 1.

Figure S1 shows the ensemble model accuracy for MRIs in the five test sets when the certainty threshold is varied — that is, when averaged measurements that tended towards 0.5 were removed and only the averages that gave consistent outputs across the ensemble were kept. See also Table 1.

Training set sites

Table S1: Sites for the training set (MGH Pre-2019), as well as the numbers of AD and Controls scanned at each

MRI Site Name	No. AD	No. CTRL	Norm AD (No. AD / Total AD)	Norm CTRL (No. CTRL / Total CTRL)	Ratio (Norm AD : Norm CTRL)
MR1WA	275	370	0.0653	0.0293	2.2243
ERMR	79	294	0.0188	0.0233	0.8041
LI_MR	135	779	0.0320	0.0618	0.5186
LI	958	5468	0.2274	0.4337	0.5243
MR3_ELL2	12	83	0.0028	0.0066	0.4327
MR1CH	196	245	0.0465	0.0194	2.3941
MR3EL2	171	472	0.0406	0.0374	1.0842
MR1W1	246	566	0.0584	0.0449	1.3007
PR62ELL2	34	129	0.0081	0.0102	0.7888
MRC40168	228	294	0.0541	0.0233	2.3208
MR1A2	142	273	0.0337	0.0217	1.5566
PR67ELL2	52	162	0.0123	0.0128	0.9606
MRFND1	228	715	0.0541	0.0567	0.9543
MR1L6	196	98	0.0465	0.0078	5.9853
MRS1OW	74	286	0.0176	0.0227	0.7743
MR2WA	89	98	0.0211	0.0078	2.7178
MR2EL2	94	238	0.0223	0.0189	1.1820
EXHDMRI	21	27	0.0050	0.0021	2.3276
MR1Y6	124	179	0.0294	0.0142	2.0731
MR2CH	149	187	0.0354	0.0148	2.3845
PR66ELL2	36	252	0.0085	0.0200	0.4275
MR1NS	161	192	0.0382	0.0152	2.5095
PR248	44	181	0.0104	0.0144	0.7275
MRC25157	44	64	0.0104	0.0051	2.0574
MR2Y6	160	284	0.0380	0.0225	1.6860
MR1NY	2	12	0.0005	0.0010	0.4988
MR1EL2	131	275	0.0311	0.0218	1.4256
CHCMRI	57	156	0.0135	0.0124	1.0935
MR3Y6	1	3	0.0002	0.0002	0.9975
MRC20597	11	52	0.0026	0.0041	0.6331
MRC35022	28	95	0.0066	0.0075	0.8820
CHCMR2	4	15	0.0009	0.0012	0.7980
GEMS	0	5	0.0000	0.0004	0.0000
MEDPC	9	12	0.0021	0.0010	2.2445
M247OC0	0	1	0.0000	0.0001	0.0000
BAY4OC	2	2	0.0005	0.0002	2.9926
BAY10W0	0	1	0.0000	0.0001	0.0000
MR3CH	11	16	0.0026	0.0013	2.0574
BAY3OC	0	8	0.0000	0.0006	0.0000
MR3WA	8	16	0.0019	0.0013	1.4963
MRS3OC0	1	2	0.0002	0.0002	1.4963
MRS5MRS5	0	1	0.0000	0.0001	0.0000
TOTAL	4213	12608	1.0000	1.0000	